ROYAL SOCIETY OF CHEMISTRY

Check for updates

# Ni crossover catalysis: truth of hydrogen evolution in Ni-rich cathode-based lithium-ion batteries†

Xingqin Wang, [ac] Dongsheng Ren,[b] Hongmei Liang,[b] Youzhi Song,[b] Hua Huo, [*a] Aiping Wang,*[b] Yunzhi Gao, [a] Jianhong Liu,[b] Yun Gao,[b] Li Wang [*b] and Xiangming He [*b]

Hydrogen in Ni-rich cathode-based batteries is always accompanied by capacity decay and safety risks. However, insights into the $H_2$ evolution have puzzled the battery community for decades. In general, solvent reduction on the anode side is considered the reason. However, we have found that it contradicts some experimental results. Herein, we experimentally demonstrate the clear pathway of $H_2$ evolution, which we call "double crossover–double catalysis" (DC–DC). The first "catalysis" occurs on the cathode side, where Ni catalyzes solvent decomposition, forming proton-containing side products. The "double crossover" indicates that the side products and dissolved nickel ions both cross to the anode side, where the nickel ion is reduced to the Ni metal catalyst. The second "catalysis" is that the Ni metal on the anode catalyzes the reduction of the proton-containing side-products, forming $H_2$. This study emphasizes the catalytic effect of Ni on both electrodes and establishes a "DC–DC" pathway for $H_2$ evolution in LIBs, shedding light on the hindrance of $H_2$ evolution in Ni-rich cathode-based batteries.

## Broader context

Understanding the fundamentals of $H_2$ evolution in Ni-rich layered oxide (NMC) based batteries plays a vital role in the improvement of the long-term cycling performance of this kind of commercial cells. Current research studies attribute the $H_2$ evolution in the early stages of the cycling to the contaminated $H_2O$, and that in the long-term cycling to the electrochemical oxidation of the electrolyte and oxygen loss in the layered cathode materials. However, the high potential and oxygen loss are not the "privileges" of the Ni-rich NMC cells, which also widely occur in the layered $LiCoO_2$-based or spinel $LiNi_{0.5}Mn_{1.5}O_4$-based cells. Intriguingly, little $H_2$ evolution is found in these cells, indicating that there must be other reasons. In this work, we demonstrate Ni catalysis on both cathode ($Ni_{lattice}$) and anode ($Ni_{metal}$) toward $H_2$ evolution by considering the crossover between electrodes. This work unambiguously demonstrates the importance of $Ni_{lattice}$ stabilization in the cathode interphasial engineering in NMC-based batteries designed for long-term cycling.

## 1. Introduction

Ni-rich layered oxide materials ($LiNi_xMn_yCo_{1−x−y}O_2$, NMC, $x \geq 0.6$) are the most promising cathode candidates for electric vehicle batteries due to their high energy density.[1,2] However, the higher Ni content results in not only a higher capacity but also more

[a] Key Laboratory of Materials for New Energy Conversion and Storage (Ministry of Industry and Information Technology, School of Chemistry and Chemical Engineering, Harbin Institute of Technology, Harbin, 150001, China. E-mail: huohua@hit.edu.cn

[b] Institute of Nuclear and New Energy Technology, Tsinghua University, Beijing, 100084, China. E-mail: aipingwang_aw@outlook.com, wang-l@tsinghua.edu.cn, hexm@tsinghua.edu.cn

[c] Risesun Mengguli New Energy Science and Technology Co., Ltd, Beijing, 102200, China

† Electronic supplementary information (ESI) available. See DOI: https://doi.org/10.1039/d2ee04109j

aggressive performance fading as a result of parasitic interfacial reactions and irreversible structure variation.[3] In addition to the commonly known phase transition and oxygen loss, gas evolution plagues NMC cells with electrolyte consumption, fast cell degradation, sudden death of the cell, or even field failure.[4–6]
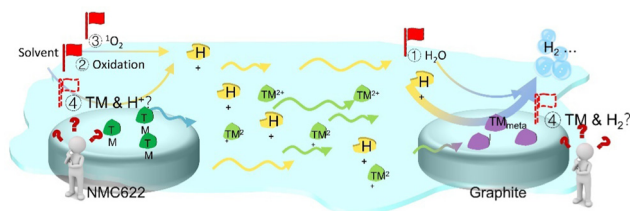
$H_2$ is the main gas detected in Ni-rich NMC cells, and much effort has been devoted to investigating its origin (Fig. 1).[7,8] In the first few cycles, $H_2$ evolution is attributed to the proton-containing contaminants,[9,10] such as $H_2O$, alcohol and acid, which are introduced during the synthesis of raw materials or cell assembly. However, in long-term cycling, $H_2$ evolution is usually attributed to cross-talk. The proton-containing side products formed at the cathode, such as HF,[11] LiH,[12–14] and the organic or solvated protons R–H+,[15,16] cross to the anode side and are reduced.[9,15,17] However, the formation of the proton-containing side products remains unclear, and the state of the side products that can be reduced to $H_2$ is ambiguous.

**1200** | *Energy Environ. Sci.*, 2023, **16**, 1200–1209

This journal is © The Royal Society of Chemistry 2023

**Paper**

Fig. 1 State-of-the-art understanding of $H_2$ evolution in Ni-rich NMC-based cells. $H^+$ represents the proton-containing side products. Direct $H_2O$ reduction and reduction of the side products from the cathode side contribute to $H_2$ evolution on the anode side. However, the formation of the side products on the cathode side remains unconvincing, and the roles of TM on both electrodes are overlooked.

Some studies have attributed the formation of proton-containing side products to electrochemical oxidation,[15] or O release from the NMC cathode (Fig. 1).[7,16,18] However, the high potential also exists in $LiNi_{0.5}Mn_{1.5}O_4$ (LNMO) cells, which can be as high as 5 V, but $H_2$ evolution is rarely reported.[19,20] $CO_2$ is the commonly reported gaseous oxidation product of carbonate

electrolytes in such cathode chemistry.[21,22] The latter, O release, is a common issue for the oxide cathode materials, such as $LiCoO_2$ (LCO)[23,24] and LNMO.[25,26] These battery chemistries have been widely reported in conjunction with O release, but have rarely been reported to occur with $H_2$ evolution.[27] As a result, a high potential and O release are far from sufficient to explain the $H_2$ evolution in Ni-rich NMC-based cells. More details concerning the side reactions on the cathode surface, which can form proton-containing side products that are ready to be reduced, need to be elucidated.

Carbonate decomposition on a transition metal (TM) oxide cathode surface has been reported to be highly correlated with the active TM and $O_{lattice}$ sites on the surface.[12-14] On the $LiNi_{0.8}Co_{0.1}Mn_{0.1}O_2$ (NMC811) surface, the dehydrogenation of ethylene carbonate (EC) was observed with *in situ* Fourier transform infrared spectroscopy.[28] Ring-opening of EC was also investigated on the LCO and $LiNi_{1/3}Co_{1/3}Mn_{1/3}O_2$ (NMC111) surfaces, where the TMs were relevant.[29] The $O_{lattice}$ has been identified as the active site for solvent oxidation on layered oxide surfaces.[30] However, the correlation of these side
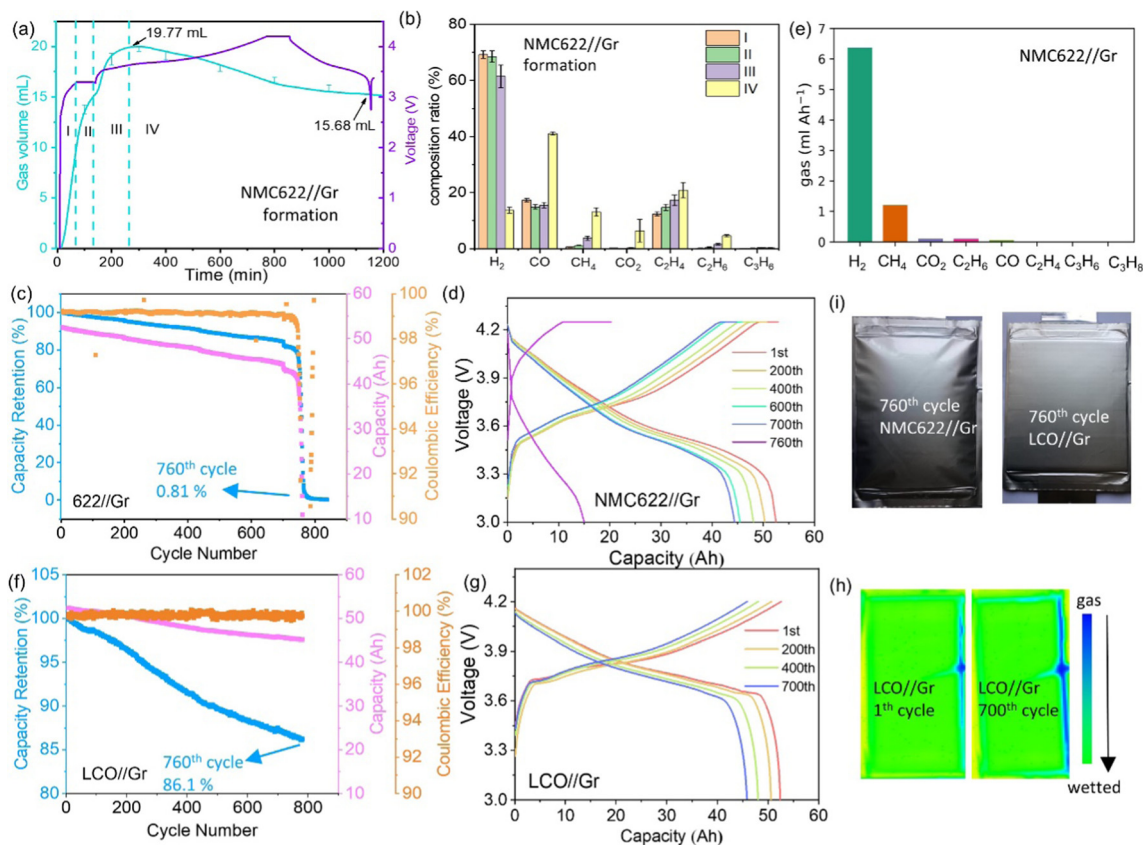


Fig. 2 Cycling performance and gas evolution of the NMC622//Gr and LCO//Gr cells. (a) Gas evolution/voltage over time at different stages, and (b) the corresponding gas component ratio measured by GC during the formation of the NMC622//Gr cell. The mean value and the standard deviation of the data from three cells during the formation were considered. (c–e) Cell performance of NMC622//Gr, which is charged and discharged at 1C between 3–4.25 V at 45 °C. (c) Cell capacity, capacity retention and Coulombic efficiency variation with cycling. (d) Voltage–capacity profiles at different cycles. (e) Gas evolution is measured by GC. Note that the gas volume is normalized to 1 A h. (f–g) Cell performance of LCO//Gr, which is charged and discharged at 1 C between 3–4.2 V at 45 °C. (f) Cell capacity, capacity retention and Coulombic efficiency variation with cycling. (g) Voltage-capacity profiles at different cycles. (h) Ultrasonic scanning images of the fresh cell and the cell after the 700th cycle. Note that the cell for ultrasonic testing is 5 A h. (i) Cell appearance of NMC622//Gr and LCO//Gr after long-term cycling.

reactions with $H_2$ evolution in Ni-rich NMC-based cells has rarely been elucidated. The concerted effects of the active sites ($TM_{lattice}$ and $O_{lattice}$) on the formation of proton-containing cell side products are not yet fully understood.

Here, we elucidate the mechanism of $H_2$ evolution in Ni-rich NMC-based LIBs through investigation of the parasitic reactions at both cathode and anode[31–33] using a combination of *ab initio* calculations and experiments. $H_2$ evolution is experimentally confirmed in the NMC cells rather than the other oxide cathode, *e.g.*, LCO. On the cathode side, the H-transfer reaction of the carbonate solvent at different active sites (both TMs and $O_{lattice}$) is explored. On the anode side, the possible active sites created by the shuttled TMs and their catalysis toward gas evolution are investigated. A "double crossover–double catalysis" (DC–DC) mechanism is proposed to explain the $H_2$ evolution, and $Ni_{lattice}$ and $O_{lattice}$ on the NMC surface are proved to be the primary cause. A mechanism based on the cell landscape for $H_2$ evolution is established, and the catalytic effect of Ni at both electrodes is emphasized. That is, the catalysis effect of Ni affects not only the formation of proton-containing side products and $H_2$ evolution, but also the solvent reduction.

## 2. Results and discussion

### $H_2$ evolution in Ni-rich NMC cells

$H_2O$, high potential and oxygen loss are usually claimed as the origin of $H_2$ evolution in Ni-rich NMC cells. We first investigated the $H_2$ evolution caused by $H_2O$ contaminants in the formation process of NMC622//Gr. As shown in Fig. 2a, we divided the gassing process into four stages (Fig. 2a). In the first three stages, the evolved gas continued to increase to a peak (19.97 mL). Then, the total evolved gas decreased, which may be attributed to cross-talk. The gas components were measured *via* gas chromatography (GC). As shown in Fig. 2b, $H_2$ is prevalent in the first three stages. However, the volume of $H_2$ dramatically decreased in stage IV, suggesting that $H_2O$ was consumed to some extent. Thus, $H_2O$ is the origin of $H_2$ evolution in the first few cycles, instead of the origin in the long-term cycling of the Ni-rich NMC-based cells. In addition to $H_2$, another interesting phenomenon is that CO and $C_2H_4$ were dominant during the formation process, while $CH_4$ was dominant after the long-term cycling. This inverse correlation was attributed to the distinct properties of the three gases.[10] The decrease of CO and $C_2H_4$ was attributed to the further reaction at the electrode/electrolyte interface, as CO is a reductive gas and $C_2H_4$ is unsaturated. However, $CH_4$ is a saturated gas and it cannot get reduced or oxidized in the cell.[34] In addition, the side reactions at the electrode/electrolyte interface would constantly generate it. These two reasons led to the accumulation of $CH_4$ after the long-term cycling.

Next, we investigated the high potential and oxygen loss. The NMC622//Gr and LCO//Gr pouch cells were designed to evaluate the $H_2$ evolution in Ni-rich NMC-based cells and the effect of the high potential and oxygen loss, as LCO has a similar or even higher redox potential than NMC-based cathode and suffers

equally from oxygen loss.[35,36] For example, the stoichiometric ratio of O/Co in LCO is 2. However, Wang *et al.* found that this ratio was lowered to 1.05 in the surface layer after high-voltage (4.6 V *vs.* $Li^+$/Li) cycling, indicating the dramatic oxygen loss.[36] As shown in Fig. 2c and d, the NMC622//Gr cell degraded linearly and dramatically decreased around the 760th cycle. This is mainly because of gas evolution and loss of active materials, according to the initial voltage of discharge/charge and the capacity during constant-voltage charge. After long-term cycling, NMC622//Gr fails at the 790th cycle, and its capacity retention was only 0.81%. In contrast, after 800 cycles, LCO//Gr still maintained a capacity retention of 86.1%. The inner state of the failed NMC622//Gr cell was detected with industrial computerized tomography (CT) (Fig. S1, ESI†). As can be seen, the electrode layers in the failed cell were separated by the evolved gas, which is the origin of the sudden rollover. The Rietveld refined XRD results (Fig. S2, ESI†) of the cycled NMC622//Gr further suggest that the electrode layered structure, both the NMC622 and Gr, was deteriorated to some extent. The (003) peak intensity of NMC622 after 500 cycles was lowered and the full width half maximum (FWHM) was expanded by 0.063° compared with the fresh one (Fig. S2a, ESI†). However, the (003) peak of LCO after 760 cycles only increased by 0.015° (Fig. S2d, ESI†). In addition, the Li/Ni mixing was increased from 1.584% to 2.018% (Fig. S2b, ESI†). These results all demonstrated the harsher electrode deterioration of NMC622.

Fig. 2i presents photographs of the two cells after long-term cycling (>700 cycles). The NMC622//Gr cell was dramatically inflated with a gas volume of ∼400 mL, while no visible gas was observed for LCO//Gr. The evolved gas of the NMC622//Gr cell was measured by GC (Fig. 2e). $H_2$ was the main gas (∼81.3 v%). $CH_4$ was the second most abundant gas, which might be attributed to the severe degradation of EMC or DMC catalyzed by the reduced $Ni_{metal}$ at the anode.[37–39] However, for LCO//Gr, as little gas was detected for GC measurements, we confirmed the slight gas production by the ultrasound technique (Fig. 2h). The gas in the cell after the 700th cycle was found to be comparable to that in the fresh cell. More ultrasonic scanning images of both cells at different cycles are shown in Fig. S3 (ESI†), further suggesting that gas evolution constantly occurred in the NMC622//Gr cell and that little occurred for the LCO//Gr cell. Moreover, while the cathode was replaced with NMC811, which has an extra 20% of Ni content than NMC622, more gas would be generated, as shown in Fig. S4 (ESI†).

In addition, the phase transition behaviors of both NMC622 and LCO cathodes were explored with the *operando* X-ray diffraction (*operando* XRD). The results indicate that NMC622 suffered more from volume change and significant side reactions (Fig. S6, ESI†). The above performance and gas evolution comparison between the NMC622//Gr cell and the LCO//Gr cell suggests that the direct electrochemical oxidation of the electrolyte cannot be responsible for the $H_2$ evolution in the NMC cells.[15,16] Additionally, $O_{lattice}$ and Co are not the primary factors causing the formation of active proton-containing side products, which direct us to the catalytic effect of Ni or Mn in the NMC cells.

**1202** | *Energy Environ. Sci.*, 2023, **16**, 1200–1209

This journal is © The Royal Society of Chemistry 2023

### Catalytic effect of TM on the cathode
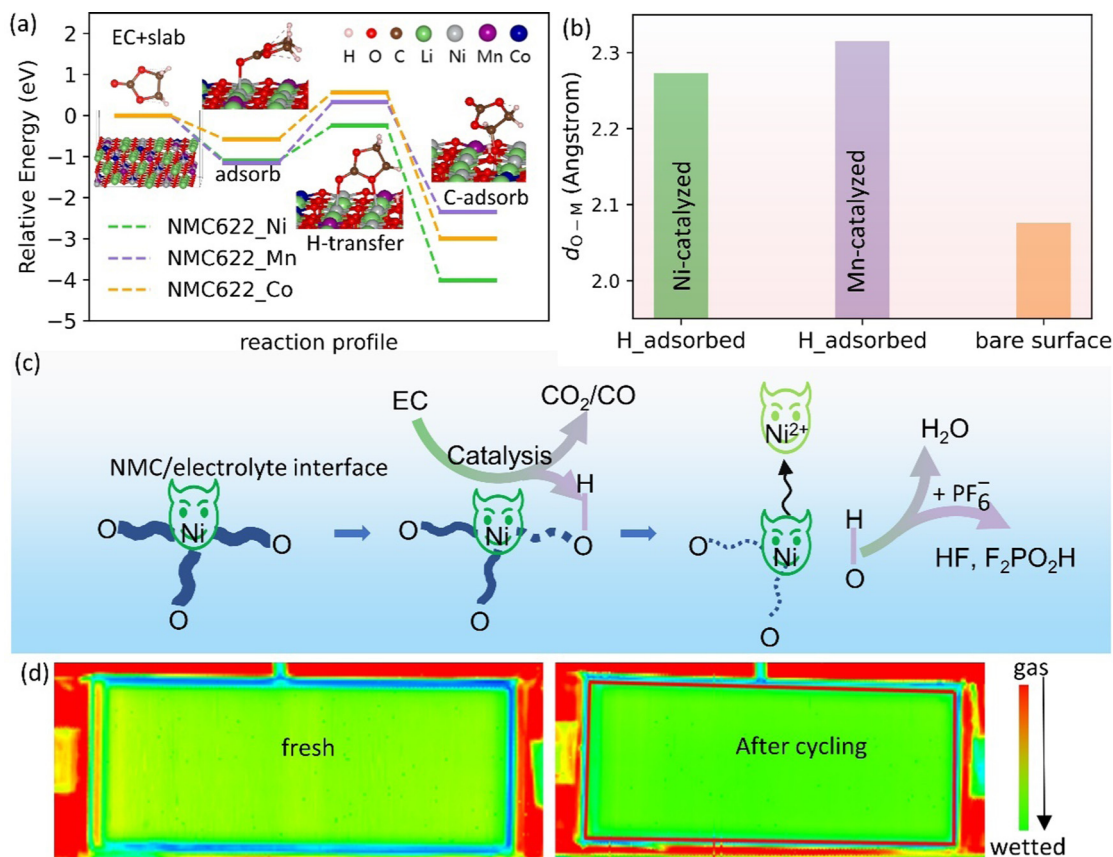
To evaluate the catalytic effect of the $TM_{lattice}$ on the NMC cathode, we explored the H-transfer process of the solvent at both the Ni and Mn sites on the NMC cathode surface, and only the catalyzed chemical reaction was considered. In addition to TMs, $O_{lattice}$ serves as an active site for the H-abstracted solvent.[30] Density functional theory (DFT) was used to explore the formation of the proton-containing side products, considering the catalytic effect of the surface Ni/Mn and $O_{lattice}$. EC was used as an example solvent, as it was reported to suffer more from H-transfer on the Ni-rich NMC cathode (*e.g.*, NMC811 and NMC622) than the low-Ni cathodes (*e.g.*, NMC111).[28] The (10$\bar{1}$4) surface was used due to its convenience for ion transport in and out (Fig. S7, ESI†).[30,40–42]

Fig. 3 shows the H-transfer pathway and the further side reaction that leads to the proton-containing side products. Fig. 3a gives the reaction profiles of the H-transfer of EC on the NMC622 surface at the $TM_{lattice}$ site in combination with the $O_{lattice}$ site. The $TM_{lattice}$ sites include $Ni_{lattice}$, $Mn_{lattice}$ and $Co_{lattice}$ sites. The H-transfer process includes three steps: solvent adsorption, H-transfer and the formation of a more stable C-adsorption geometry from which H is abstracted.[28]

It should be noted that the path only focuses on H-transfer without considering the further decomposition of EC, which might transform to other side products such as $CO_2$. The geometries along the reaction path at the $Ni_{lattice}$ site are presented in Fig. 3a, and those at the $Mn_{lattice}$ and $Co_{lattice}$ sites are shown in Fig. S8 (ESI†). The reaction energy difference of the H-transfer step ($\Delta E_{H\text{-transfer}}$) was used to describe the catalytic effect of the $TM_{lattice}$. As shown in Fig. 3a, the $Ni_{lattice}$ site shows the lowest reaction energy for the H-transfer process and $Co_{lattice}$ shows the highest reaction energy, indicating the most significant catalytic effect of $Ni_{lattice}$ on H-transfer during the EC decomposition.

Moreover, the distinct amounts of exposed active sites of NMC622 and LCO are also a reason for more significant side reactions at the NMC622/electrolyte interface. As indicated in Fig. S9 (ESI†), NMC622 exhibited a smaller particle size and thus a larger specific area, which inevitably would result in more side reactions at the NMC622/electrolyte interface.

Furthermore, the stability of the $O_{lattice}$ accepting the H was analyzed by measuring the bond length with the surrounding metal ions (lattice TMs and Li), denoted as $d_{O-M}$. As shown in Fig. 3b, the length of the $OH_{lattice}$ bond with metal ions is ~2.3 Å,



**Fig. 3** Catalytic effect of $TM_{lattice}$ (Ni/Mn/Co) toward side reactions that lead to proton-containing products on the cathode side. (a) H-transfer reaction profile of EC at the $Ni_{lattice}$, $Mn_{lattice}$ and $Co_{lattice}$ sites on the NMC622 (10$\bar{1}$4) surface. The reaction process at $Ni_{lattice}$ is shown. (b) Bond length between the metal ions (lattice TMs and Li) and the $O_{lattice}$ with and without accepting a proton from the solvent. (c) A scheme for $Ni_{lattice}$ catalysis and the release of TM ions on the cathode side. (d) Ultrasonic scanning images of the LCO//Gr–Ni cell before and after cycling. Gr–Ni dictates that the anode was disassembled from the $H_2$-evolved NMC cell.

This journal is © The Royal Society of Chemistry 2023

*Energy Environ. Sci.*, 2023, **16**, 1200–1209 | **1203**

longer than that of the bare surface structure ($\sim 2$ Å), indicating weaker bonding between the $OH_{lattice}$ and the NMC cathode. In addition to the H-transfer of solvent on the cathode, the resulting unstable $OH_{lattice}$ on the cathode surface would undergo other side reactions, such as the formation of $H_2O$,[43] or $HF/F_2PO_2H$, once $PF_6^-$ is present,[11,44,45] as shown in Fig. 3c. As a result, transport of the proton-containing side products catalyzed by $TM_{lattice}$ and $O_{lattice}$ on the cathode to the anode are responsible for the $H_2$ evolution in NMC cells. Moreover, the hole left due to the desorption of $OH_{lattice}$ would lead to the instability of the TMs on the surface, facilitating TM dissolution and decreasing cell performance.

To confirm that the proton-containing side products are generated from the cathode side, we used the Gr anode disassembled from the NMC//Gr cell, which had evolved $H_2$ to reassemble a new cell coupled with LCO. The reassembled cell was noted as LCO//Gr–Ni, as it was deposited with Ni and Mn elements. The ultrasonic scanning images of the LCO//Gr–Ni cell before and after the long-term cycling (more than 300 cycles) are shown in Fig. 3d. After the long-term cycling, the cell remained wetted, suggesting that no $H_2$ was evolved. The only difference between the original NMC//Gr and the reassembled NMC//Gr–Ni was the cathode where no catalysis effect of $Ni_{lattice}$ exists. The result further demonstrated that the proton source came from the catalyzed solvent decomposition by Ni and Mn on the cathode.

**Catalytic effect of TM on the anode**

The anode side, where the shuttled proton-containing species are reduced,[15] is also where the shuttled TM ions deposit and may participate in the formation of the SEI.[46] The TM ion/metal on the graphite surface was measured by ICP, as shown in Fig. 4a. Ni was the most abundant, while Co was the least abundant, consistent with the reported results.[47] The table in the figure inset shows the values directly detected, as well as the accumulation rate.
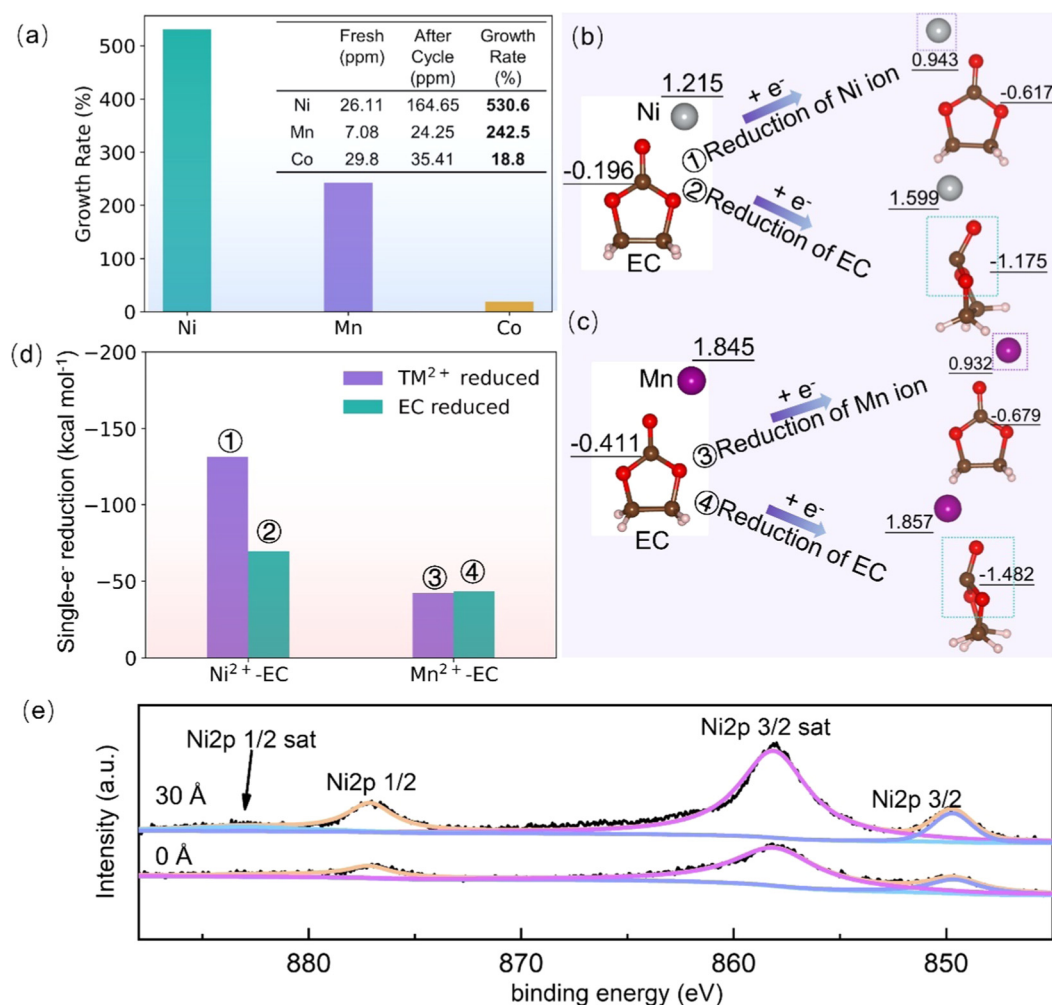


Fig. 4 Study on the valence state of shuttled TMs on the anode side. (a) TM growth rate compared with the fresh anode measured by ICP. (b) and (c) show the single-$e^-$ reduction processes of the $Ni^{2+}$–EC and $Mn^{2+}$–EC clusters, respectively. The NPA charges of the TM and carbonate group ($CO_3$) are noted. The reduced parts are emphasized with dotted boxes. (d) Reduction energies for the reactions in (b) and (c). (e) XPS spectra of the anode after 500 cycles at the SEI depth of 0 Å and 30 Å. Binding energy of the Ni element is consistent with that of the Ni metal, and the Ni ion is prone to be reduced at the inner side of SEI. The color code is as described in Fig. 3.

**1204** | *Energy Environ. Sci.*, 2023, **16**, 1200–1209

This journal is © The Royal Society of Chemistry 2023

Ni metal is a high-performing electrocatalyst for the $H_2$ evolution reaction (HER) in the field of clean hydrogen energy.[48,49] This prompted us to investigate the role of TM ions in $H_2$ evolution. Before this exploration, we should determine the valence state of the TMs at the anode side.[50] To do so, we calculated the single-$e^-$ reduction of the $TM^{2+}$–solvent clusters to evaluate whether the TM ions or solvent molecule would be reduced. $Ni^{2+}$, $Mn^{2+}$ and EC were all evaluated.

Fig. 4b–d shows the single-$e^-$ reduction of the two $TM^{2+}$–solvent clusters ($Ni^{2+}$–EC and $Mn^{2+}$–EC). The reduced parts (TMs or the carbonate group ($CO_3$)) are indicated by dotted boxes, and their natural population analysis (NPA) charges are noted. According to the single-$e^-$ reduction energy, the $Ni^{2+}$–EC cluster prefers to be reduced compared to the $Mn^{2+}$–EC cluster. Moreover, as shown in Fig. 4d, for the $Ni^{2+}$–EC cluster, the single-$e^-$

reduction energy of $Ni^{2+}$ was $-131.35$ kcal mol$^{-1}$, approximately twice of that of EC, suggesting that Ni metal will form at the anode side. This was further confirmed by the X-ray photoelectron spectroscopy (XPS) in Fig. 4e.[51] In addition, the Ni metal intensity in the SEI at the depth of 30 Å was higher than that of the SEI surface (0 Å), indicating the easier reduction of Ni ions at the inner part of the SEI where electron tunneling is possible. In addition to the XPS results, the Ni metal was also observed by the cryogenic electron microscope (Cryo-EM).[50] However, for the $Mn^{2+}$–EC cluster, the single-$e^-$ reduction energies of different parts ($Mn^{2+}$ or EC) were comparable, suggesting that $Mn^{2+}$ prefers to exist in the SEI as a divalent state. This conclusion is also consistent with previous reports.[46,52]

To further confirm the catalytic effect of $Ni_{metal}$ on $H_2$ evolution, the Volmer–Heyrovsky $H_2$ evolution processes on
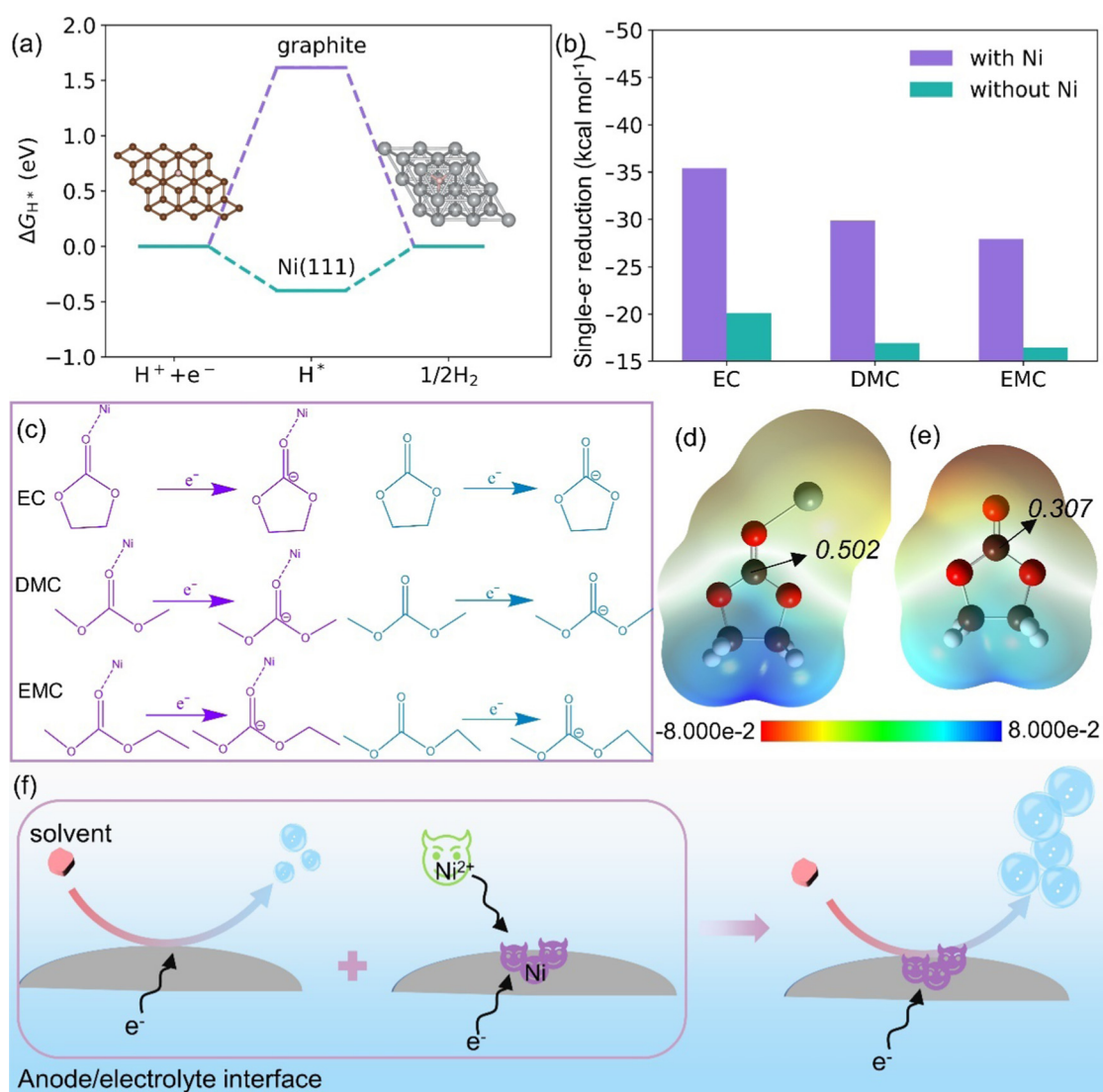


Fig. 5 Catalytic effect of the Ni metal toward $H_2$ evolution and solvent reduction on the anode side. (a) Reaction profile for the Volmer–Heyrovsky mechanism of $H_2$ evolution on graphite and the Ni (111) surface. The insets show the adsorption of H* on the top-site of the graphite (left) and hollow-site of the Ni (111) (right) surface. (b) Single-$e^-$ reduction of three common carbonate solvents (EC, DMC and EMC) with and without Ni. (c) Reduction reactions in (b). Electrostatic potential of EC with (d) and without (e) nearby Ni. The Mulliken charge of the carbonyl carbon is marked on the contour surface structure. (f) A scheme for the aggravated gas evolution induced by the reduced Ni metal. The color code is consistent with Fig. 3.

both graphite and Ni (111) surface were calculated. As shown in Fig. 5a, the H adsorption on the Ni (111) surface was much closer to 0, indicating that Ni is a better catalyst for $H_2$ evolution.[49,53] Given that a large amount of Ni exists at the anode (Fig. 4a), this result further explains why the $H_2$ evolution is aggravated in the Ni-rich NMC LIBs.

In addition to the $H_2$ evolution catalyzed by $Ni_{metal}$, the dramatic gas evolution in Ni-rich NMC-based LIBs caused us to suspect that the $Ni_{metal}$ on the anode might also catalyze the reduction of other solvents.[7,8,17,18] To confirm this, we calculated the single-$e^-$ reduction of the solvent molecule, with and without $Ni_{metal}$. As shown in Fig. 5b and c, the single-$e^-$ reduction energy of the Ni–solvent cluster (indicated in purple) was much lower than that of the isolated molecule (indicated in blue). The reduced structures are shown in Fig. S10 and S11 (ESI†) in a ball-and-stick model. Furthermore, we found that the easier reduction of the cluster could be attributed to the increased positive charge on the carbonyl carbon caused by $Ni_{metal}$ and the more separated positive and negative charges on the solvent molecule (Fig. 5d and e). Simultaneously, the separated charges facilitate the reduction of the carbonyl carbon. Similar results were also found in DMC and EMC systems (Fig. S12 and S13, ESI†). As demonstrated, the $Ni_{metal}$ on the anode not only aggravates the $H_2$ evolution and solvent decomposition, but also inhibits the SEI regeneration due to the constant bubbling on the anode. Fig. 5f shows a scheme of the aggravated gas evolution on the anode side catalyzed by the reduced Ni metal. Although expected because of the high energy density of the NMC cathode, the catalysis of $Ni_{metal}$ toward the $H_2$ evolution and solvent decomposition indicates that the protection of the active sites on the NMC cathode is of priority to eliminate the H-transfer and the subsequent TM dissolution.

### Inactivation of the $TM_{lattice}$ *via* LiDFP

Furthermore, to inactivate the catalytic sites, we covered the active sites with lithium diflurophosphate (LiDFP, $LiPO_2F_2$) on the cathode surface in a theoretical model. The adsorption energies of $PO_2F_2$ on the $Ni_{lattice}$ and $Mn_{lattice}$ sites were found to be as low as $-2.42$ and $-3.02$ eV, respectively (Fig. S14, ESI†). The bond length between the TM and the O in $PO_2F_2$ was $\sim 2.0$ Å, similar to the TM–O bond length in the bulk phase, suggesting that a chemical bond was formed between the TM and $PO_2F_2$. With such strong bonding, we predict that the coverage of the active sites can protect the electrolyte and stabilize the cathode by inhibiting the $O_{lattice}$ loss and TM dissolution. This was further experimentally demonstrated, and the results are presented in Fig. S15 (ESI†). As can be seen, the $H_2$ evolution after the addition of LiDFP has been dramatically suppressed, and the cell preserved a higher capacity retention (77.41%) than that without LiDFP (73.37%) after 480 cycles.

Based on the above results, we proposed a "double crossover–double catalysis" (DC–DC) mechanism for $H_2$ evolution in NMC cells. In detail, "Double crossover" describes the proton-containing species and the dissolved TM ion transport to the anode side. "Double catalysis" describes the concerted catalytic

effect of $Ni_{lattice}$ and $O_{lattice}$ on the cathode surface toward the H-transfer, and the catalytic effect of $Ni_{metal}$ on the anode toward the $H_2$ evolution and the reduction of solvents.

## 3. Conclusion

In this work, we disclose the pathway of $H_2$ evolution based on cross-experiments among Ni-rich, Ni-free cathodes, Gr anode and Ni@Gr anode, where the Ni@Gr anode is the Gr anode disassembled from NMC//Gr cell. Ni@Gr has been deposited with Ni. Furthermore, the *ab initio* calculations are applied to verify the key chemical reactions in the pathway. We found that Ni on the cathode and that deposited on the anode work together to catalyze the $H_2$ evolution in Ni-rich NMC LIBs. Ni on the anode comes from the cathode by crossover. If there is no Ni on any electrode, $H_2$ evolution cannot happen. On the cathode side, Ni catalyzes the formation of proton-containing side products and aggravates TM dissolution. These side products cross over to the anode side, as well as the dissolved Ni ions. On the anode side, the Ni ions are then reduced to produce $H_2$ by catalysis of Ni deposited on the anode. We call the above $H_2$ evolution process as "double crossover–double catalysis" (DC–DC). The "double crossover" indicates both Ni and proton-containing side products cross over from cathode to anode. The "double catalysis" indicates that Ni catalysis takes place on both cathode and anode. Our work highlights the catalytic effect of Ni on $H_2$ evolution in Ni-rich NMC-based LIBs, indicating that inactivation of the catalytic TM sites is the primary strategy to inhibit $H_2$ evolution. In addition, the membrane design and anode surface modification can be combined to further cut off the crosstalk between the electrodes and achieve a superior Ni-rich NMC-based battery.

## 4. Computational and experimental procedures

### Computational details

The calculations of the isolated systems were performed with Gaussian 16 (Revision C.01). All systems were optimized at the level of B3LYP/6-31g*. The dispersion interaction was corrected with GD3BJ for all calculations. The SMD implicit solvation model was used with the parameter input of acetonitrile. The single point energies were calculated at the level of TPSSh/def2TZVP. The solvation free energies were calculated at the level of M05-2X/6-31g*. The Gibbs free energy was corrected with zero-point energy and thermal energy. The charge distribution was analyzed with natural population analysis (NPA). $3d^5$ and $3d^8$ were chosen as the outmost electrons in DFT calculation for $Mn^{2+}$ and $Ni^{2+}$, respectively.

The periodic calculations were performed with the Vienna Ab initio Simulation Package (VASP). Projector plane wave (PAW) method was used to describe the core-valence electron interaction. The electron interaction was described with Perdew–Burke–Ernzerhof (PBE) generalized gradient approximation (GGA). The cut-off energy was 400 eV. The K mesh was sampled

**1206** | *Energy Environ. Sci.*, 2023, **16**, 1200–1209

This journal is © The Royal Society of Chemistry 2023

with $1 \times 1 \times 1$ for optimization and $4 \times 4 \times 1$ for static calculation. The tolerance of the structural relaxation and the electronic self-consistent iteration were set to 0.05 eV $\text{Å}^{-1}$ and $10^{-4}$ eV, respectively. Spin-polarization was performed for all calculations. The vdW interaction was corrected with DFT-GD3BJ method.[54,55] Hubbard U corrections (GGA + U) of the transition metals were considered and the U values of Mn, Co, and Ni were set as 4.64 eV, 4.91 eV, and 6.70 eV, respectively.[56,57] Valence electrons were $1s^2 2s^1$ for Li, $2s^2 2p^4$ for O, $3p^6 3d^9 4s^1$ for Ni, $3p^6 3d^6 4s^1$ for Mn, $3d^8 4s^1$ for Co, $2s^2 2p^2$ for C and $1s^1$ for H.

The surface model of NMC622 was constructed by a $(3 \times 3)$ supercell containing 192 atoms with a formula of $Li_{48}(Ni_{28}Mn_{10}Co_{10})O_{96}$ (Fig. S7, ESI†). The Ni, Co and Mn were randomly distributed in the transition metal lattice site.[57] The surface plane $(10\bar{1}4)$ was studied as it is a convenient ion transport and has the lowest surface energy among the low index surfaces, like the $(10\bar{1}0)$ and $(11\bar{2}0)$.[30,40–42] Two bottom layers of the slab were fixed as the bulk structure. The length of the vacuum space along the z-axis perpendicular to $(10\bar{1}4)$ of the super cell was $\sim 18$ Å to avoid spurious interactions between slabs. $PO_2F_2$ was optimized with a cell of $19 \times 20 \times 21$ $\text{Å}^3$. The adsorption energy was calculated by $E = E_{NMC+PO_2F_2} - E_{NMC} - E_{PO_2F_2}$ in the neutral state.

The graphite (001) and Ni metal (111) surface models were constructed as a $(3 \times 3)$ supercell, containing 36 and 45 atoms, respectively. The calculation procedure for the Gibbs free energy of H-adsorption was consistent with previous work.[48,49] The zero-point energy and entropy concerned item were set to 0.05 eV and 0.2 eV, respectively. All structural visualizations were performed with VESTA.[58]

### Experimental details

The pouch cells were manufactured by Risesun Mengguli New Energy Science and Technology Co., Ltd. Two active materials, $LiNi_{0.6}Mn_{0.2}Co_{0.2}O_2$ (NMC622) and $LiCoO_2$ (LCO), were used as the cathode. The anode active materials were all identical artificial graphite (Gr). Two different cells were prepared with these active materials, which were NMC622//Gr and LCO//Gr. The electrolyte was prepared with 1 mol $L^{-1}$ lithium hexafluorophosphate ($LiPF_6$) dissolved in mixed solvents of EC/EMC/DMC $(1:1:1$ by volume), and 1 wt% vinylene carbonate (VC) was added as the additive for better solid electrolyte interphase formation. A polyethylene membrane coated with ceramic was used. More details of the cells are presented in Table S1 (ESI†).

The electrochemical cycling performance of all cells was tested on a CT3001 B tester (Wuhan Land Electronic Co., Ltd). The tests of NMC//Gr he LCO//Gr were conducted in a potential range of 3–4.25 V and 3–4.2 V, respectively, at 1C and 45 °C. The TM content on the anode surface was quantitatively measured by inductively coupled plasma optical emission spectrometer (ICP-OES Agilent 5110, Agilent Technologies Co. Ltd). Gas volume during the formation process was measured with a home-made *operando* pressure detector (Fig. S16, ESI†). The cell was clamped with two plates during the test to assure the full collection of the gas. Gas components were measured by gas chromatography (2010 plus, Shimadzu Co. Ltd). The ultrasonic

scanning images were taken with an Ultrasonic Scanning System (UBSC-LD40). The phase evolutions of the cathodes were conducted using *operando* X-ray diffraction (*operando* XRD, Bruker D8) in half cells. Cross-sectional images of the battery were performed with industrial computerized tomography (CT) (RMCT4000, Royma tech). The valence state of Ni on the anode was confirmed by X-ray photoelectron spectroscopy (XPS) (Thermo Scientific Nexsa), and the sputtering rate was 0.1 nm $s^{-1}$.

## Data availability statement

The data that support the findings of this study are available from the corresponding authors upon reasonable request.

## Conflicts of interest

The authors declare no conflicts of interest.

## References

1 J. Liu, J. Wang, Y. Ni, K. Zhang, F. Cheng and J. Chen, *Mater. Today*, 2021, **43**, 132–165.
2 G. M. Hobold, J. Lopez, R. Guo, N. Minafra, A. Banerjee, Y. Shirley Meng, Y. Shao-Horn and B. M. Gallant, *Nat. Energy*, 2021, **6**, 951–960.

This journal is © The Royal Society of Chemistry 2023

*Energy Environ. Sci.*, 2023, **16**, 1200–1209 | **1207**

3  A. Chakraborty, S. Kunnikuruvan, S. Kumar, B. Markovsky, D. Aurbach, M. Dixit and D. T. Major, *Journal*, 2020, **32**, 915–952.

4  Q. Xie, Z. Cui and A. Manthiram, *Adv. Mater.*, 2021, **33**, e2100804.

5  G. Qian, J. Wang, H. Li, Z.-F. Ma, P. Pianetta, L. Li, X. Yu and Y. Liu, *Natl. Sci. Rev.*, 2021, 9.

6  Y. Jin, Z. Zheng, D. Wei, X. Jiang, H. Lu, L. Sun, F. Tao, D. Guo, Y. Liu, J. Gao and Y. Cui, *Joule*, 2020, **4**, 1714–1729.

7  H. Zhao, J. Wang, H. Shao, K. Xu and Y. Deng, *Energy Environ. Mater.*, 2021, **5**, 327–336.

8  B. Rowden and N. Garcia-Araez, *Energy Rep.*, 2020, **6**, 10–18.

9  E. R. Logan, H. Hebecker, A. Eldesoky, A. Luscombe, M. B. Johnson and J. R. Dahn, *J. Electrochem. Soc.*, 2020, 167.

10  L. D. Ellis, J. P. Allen, L. M. Thompson, J. E. Harlow, W. J. Stone, I. G. Hill and J. R. Dahn, *J. Electrochem. Soc.*, 2017, **164**, A3518–A3528.

11  M. Liu, J. Vatamanu, X. Chen, L. Xing, K. Xu and W. Li, *ACS Energy Lett.*, 2021, **6**, 2096–2102.

12  L. Huang, G. Xu, X. Du, J. Li, B. Xie, H. Liu, P. Han, S. Dong, G. Cui and L. Chen, *Adv. Sci.*, 2021, **8**, 2100676.

13  G. Xu, J. Li, C. Wang, X. Du, D. Lu, B. Xie, X. Wang, C. Lu, H. Liu, S. Dong, G. Cui and L. Chen, *Angew. Chem., Int. Ed.*, 2021, **60**, 7770–7776.

14  Z. Shadike, H. Lee, O. Borodin, X. Cao, X. Fan, X. Wang, R. Lin, S. M. Bak, S. Ghose, K. Xu, C. Wang, J. Liu, J. Xiao, X. Q. Yang and E. Hu, *Nat. Nanotechnol.*, 2021, **16**, 549–554.

15  M. Metzger, B. Strehle, S. Solchenbach and H. A. Gasteiger, *J. Electrochem. Soc.*, 2016, **163**, A798–A809.

16  J. Hu, L. Li, Y. Bi, J. Tao, J. Lochala, D. Liu, B. Wu, X. Cao, S. Chae, C. Wang and J. Xiao, *Energy Storage Mater.*, 2022, **47**, 195–202.

17  B. B. Berkes, A. Schiele, H. Sommer, T. Brezesinski and J. Janek, *J. Solid State Electrochem.*, 2016, **20**, 2961–2967.

18  N. E. Galushkin, N. N. Yazvinskaya and D. N. Galushkin, *J. Electrochem. Soc.*, 2019, **166**, A897–A908.

19  C. Zhan, T. Wu, J. Lu and K. Amine, *Energy Environ. Sci.*, 2018, **11**, 243–257.

20  H. Li, R. Fong, M. Woo, H. Ahmed, D.-H. Seo, R. Malik and J. Lee, *Joule*, 2022, **6**, 53–91.

21  K. W. Leitner, H. Wolf, A. Garsuch, F. Chesneau and M. Schulz-Dobrick, *J. Power Sources*, 2013, **244**, 548–551.

22  A. Kajiyama, R. Masaki, T. Wakiyama, K. Matsumoto, A. Yoda, T. Inada, H. Yokota and R. Kanno, *J. Electrochem. Soc.*, 2015, **162**, A1516–A1522.

23  F.-M. Wang, E. B. Chemere, W.-C. Chien, C.-L. Chen, C.-C. Hsu, N.-H. Yeh, Y.-S. Wu, C. Khotimah, K. W. Guji and L. Merinda, *ACS Appl. Mater. Interfaces*, 2021, **13**, 46703–46716.

24  W. Kong, J. Zhang, D. Wong, W. Yang, J. Yang, C. Schulz and X. Liu, *Angew. Chem., Int. Ed.*, 2021, **60**, 27102–27112.

25  E. Hu, S.-M. Bak, J. Liu, X. Yu, Y. Zhou, S. N. Ehrlich, X.-Q. Yang and K.-W. Nam, *Chem. Mater.*, 2014, **26**, 1108–1118.

26  L. Cai, Z. Liu, K. An and C. Liang, *J. Mater. Chem. A*, 2013, **1**, 6908–6914.

27  B. Michalak, B. B. Berkes, H. Sommer, T. Bergfeldt, T. Brezesinski and J. Janek, *Anal. Chem.*, 2016, **88**, 2877–2883.

28  Y. Zhang, Y. Katayama, R. Tatara, L. Giordano, Y. Yu, D. Fraggedakis, J. G. Sun, F. Maglia, R. Jung, M. Z. Bazant and Y. Shao-Horn, *Energy Environ. Sci.*, 2020, **13**, 183–199.

29  X. Qin, P. B. Balbuena and M. Shao, *J. Phys. Chem. C*, 2019, **123**, 14449–14458.

30  T. M. Østergaard, L. Giordano, I. E. Castelli, F. Maglia, B. K. Antonopoulos, Y. Shao-Horn and J. Rossmeisl, *J. Phys. Chem. C*, 2018, **122**, 10442–10449.

31  G. Zhou, X. Sun, Q. H. Li, X. Wang, J. N. Zhang, W. Yang, X. Yu, R. Xiao and H. Li, *J. Phys. Chem. Lett.*, 2020, **11**, 3051–3057.

32  K. Leung, *Chem. Mater.*, 2017, **29**, 2550–2562.

33  T. Joshi, K. Eom, G. Yushin and T. F. Fuller, *J. Electrochem. Soc.*, 2014, **161**, A1915–A1921.

34  Y. Wang, X. Feng, Y. Peng, F. Zhang, D. Ren, X. Liu, L. Lu, Y. Nitta, L. Wang and M. Ouyang, *Joule*, 2022, **6**, 906–922.

35  C. Sun, X. Liao, F. Xia, Y. Zhao, L. Zhang, S. Mu, S. Shi, Y. Li, H. Peng, G. Van Tendeloo, K. Zhao and J. Wu, *ACS Nano*, 2020, **14**, 6181–6190.

36  J. Wang, R. Chen, L. Yang, M. Zan, P. Chen, Y. Li, W. Li, H. Yu, X. Yu, X. Huang, L. Chen and H. Li, *Adv. Mater.*, 2022, **34**, 2200655.

37  Y. Wang, S. Nakamura, M. Ue and P. B. Balbuena, *J. Am. Chem. Soc.*, 2001, **123**, 11708–11718.

38  K. Tasaki, *J. Phys. Chem. B*, 2005, **109**, 2920–2933.

39  Y. X. Wang and P. B. Balbuena, *Int. J. Quantum Chem.*, 2005, **102**, 724–733.

40  D. Kramer and G. Ceder, *Chem. Mater.*, 2009, **21**, 3799–3809.

41  S. Xu, G. Luo, R. Jacobs, S. Fang, M. K. Mahanthappa, R. J. Hamers and D. Morgan, *ACS Appl. Mater. Interfaces*, 2017, **9**, 20545–20553.

42  M. Lin, X. Yang, X. Zheng, J. Zheng, J. Cheng and Y. Yang, *J. Electrochem. Soc.*, 2021, **168**, 050505.

43  R. Jung, M. Metzger, F. Maglia, C. Stinner and H. A. Gasteiger, *J. Phys. Chem. Lett.*, 2017, **8**, 4820–4825.

44  C. Jayawardana, N. Rodrigo, B. Parimalam and B. L. Lucht, *ACS Energy Lett.*, 2021, **6**, 3788–3792.

45  A. T. S. Freiberg, M. K. Roos, J. Wandt, R. De Vivie-Riedle and H. A. Gasteiger, *J. Phys. Chem. A*, 2018, **122**, 8828–8839.

46  C. Wang, L. Xing, J. Vatamanu, Z. Chen, G. Lan, W. Li and K. Xu, *Nat. Commun.*, 2019, **10**, 3423.

47  X.-Q. Zhang, X.-M. Wang, B.-Q. Li, P. Shi, J.-Q. Huang, A. Chen and Q. Zhang, *J. Mater. Chem. A*, 2020, **8**, 4283–4289.

48  J. Hu, S. Zheng, X. Zhao, X. Yao and Z. Chen, *J. Mater. Chem. A*, 2018, **6**, 7827–7834.

49  B. Zhang, X. Fu, L. Song and X. Wu, *Phys. Chem. Chem. Phys.*, 2020, **22**, 25685–25694.

50  R. A. Vilá, W. Huang and Y. Cui, *Cell Rep. Phys. Sci.*, 2020, **1**, 100188.

51  A. M. Venezia, R. Bertoncello and G. Deganello, *Surf. Interface Anal.*, 1995, **23**, 239–247.

52  C. Zhan, J. Lu, A. Jeremy Kropf, T. Wu, A. N. Jansen, Y. K. Sun, X. Qiu and K. Amine, *Nat. Commun.*, 2013, **4**, 1–8.

53  B. Zhang, X. Fu, L. Song and X. Wu, *Carbon*, 2021, **172**, 122–131.

54  S. Grimme, J. Antony, S. Ehrlich and H. Krieg, *J. Chem. Phys.*, 2010, **132**, 154104.

55 S. Grimme, S. Ehrlich and L. Goerigk, *J. Comput. Chem.*, 2011, **32**, 1456–1465.

56 V. I. Anisimov, J. Zaanen and O. K. Andersen, *Phys. Rev. B: Condens. Matter Mater. Phys.*, 1991, **44**, 943–954.

57 C.-C. Su, M. He, J. Shi, R. Amine, Z. Yu, L. Cheng, J. Guo and K. Amine, *Energy Environ. Sci.*, 2021, **14**, 3029–3034.

58 K. Momma and F. Izumi, *J. Appl. Crystallogr.*, 2011, **44**, 1272–1276.

This journal is © The Royal Society of Chemistry 2023

*Energy Environ. Sci.*, 2023, **16**, 1200–1209 | **1209**